Particle Physics at CERN

Annual Report 2012

SNF* and FORCE† grants

C. Amsler[‡] V. Chiochia[§] C. Regenfus[§] P. Robmann[§]

May 6, 2013

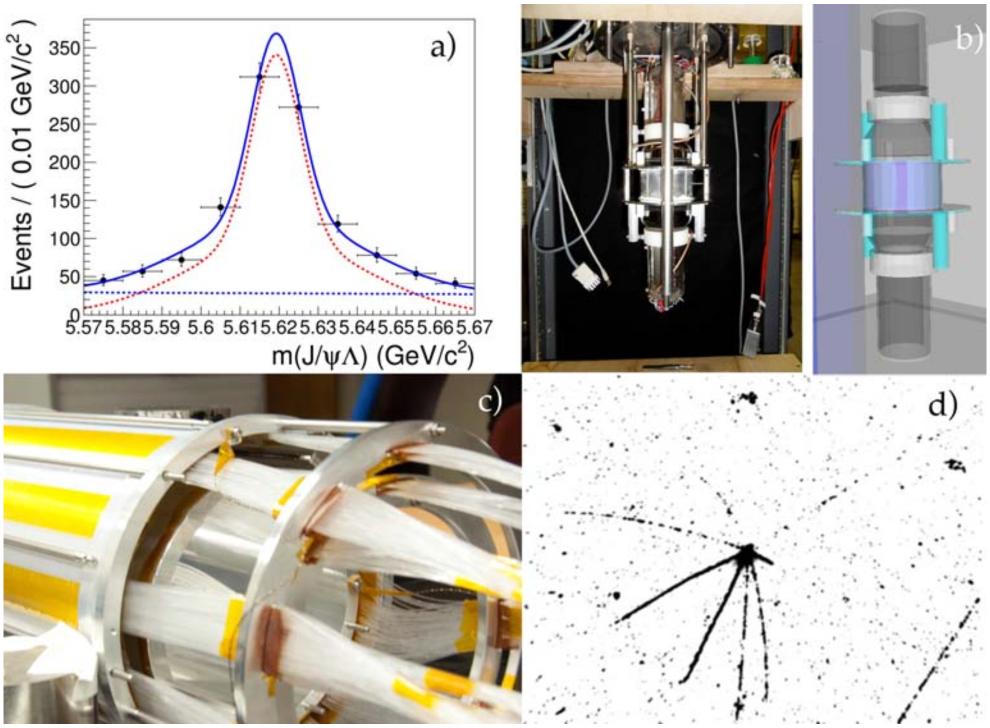

---

[*] 200020_134620

[†] 206620_141302

[‡] Principal investigator

[§] Co-applicant

Contents

This report covers the activities of our group between 1 April 2012 and 31 March 2013. At CERN we were involved in the AEgIS and CMS experiments. Data taking for the DIRAC experiment was completed in 2012. Some of us performed detector developments for dark matter searches in liquid argon (DARWIN-consortium) and for a measurement of the gravitational acceleration of antihydrogen (CERN-AEgIS Collaboration). The three PhD students supported by the grants are due to submit their theses in June 2013. The P.I. also contributed to the 2012 release of the "Review of Particle Physics" (Particle Data Group). Further details can be obtained from http://cern.ch/amsler/ and http://cern.ch/chiochia/. Since August 2012 the P.I. is Professor Emeritus and is associated as Senior Staff with the Albert Einstein Center for Fundamental Physics (Laboratory for High Energy Physics) of the University of Bern.

Cover picture:
a) J/ψ Λ-invariant mass with fit (full curve) showing the Λ_b observed by CMS. The signal and background contributions are shown separately by the dashed lines;
b) Liquid argon cell (left) and Monte Carlo model (right) to measure the light yield from neutron induced nuclear recoils;
c) Fast Annihilation Tracking (FACT) scintillation fiber detector for AEgIS;
d) Antiproton annihilation observed in a nuclear emulsion (R&D for AEgIS).

1 Particle physics with CMS

E. Aguiló, C. Amsler, V. Chiochia, S. de Visscher, C. Favaro, M. Ivova Rikova, B. Millán Mejías, P. Robmann, H. Snoek, M. Verzetti

and the CMS Collaboration.

The search for the Higgs boson was one of the main motivations for the construction of the Large Hadron Collider. The most important result in 2012 was of course the discovery at 125 GeV of a new particle compatible with the Higgs boson, decaying into two photons and four leptons (via Z^0Z^0 and W^+W^-). The published data [1] were taken in 2011 and 2012 at 7 and 8 TeV with an integrated luminosity of about 10 fb^{-1}. Figure 1.1 shows the $\gamma\gamma$ invariant mass distribution with a clear signal around 125 GeV. In the four-lepton channels CMS observed 9 events, while expecting a background of 3.8 ± 0.5 events and 7.5 ± 0.9 signal events for a standard model (SM) Higgs boson of 125 GeV (for ATLAS the numbers are compatible). Comparing with the SM we find at CMS a ratio of measured to predicted signal of 0.87 ± 0.23 while ATLAS finds 1.4 ± 0.3. The mass is 125.3 ± 0.6 GeV (CMS) and 126.0 ± 0.6 GeV (ATLAS). The spin of the new boson is not firmly established but is restricted by the $\gamma\gamma$ channel to 0^{++} or 2^{++}, although 0^{++} is preferred, as expected for a SM Higgs. The spin can be determined for instance by analyzing the correlations between lepton pairs in the $Z^0Z^0 \rightarrow 4e$ channel [2]. This, however, requires larger data samples.

In 2012 the LHC delivered 23 fb^{-1} at 8 TeV before being shut down for maintenance until 2015.

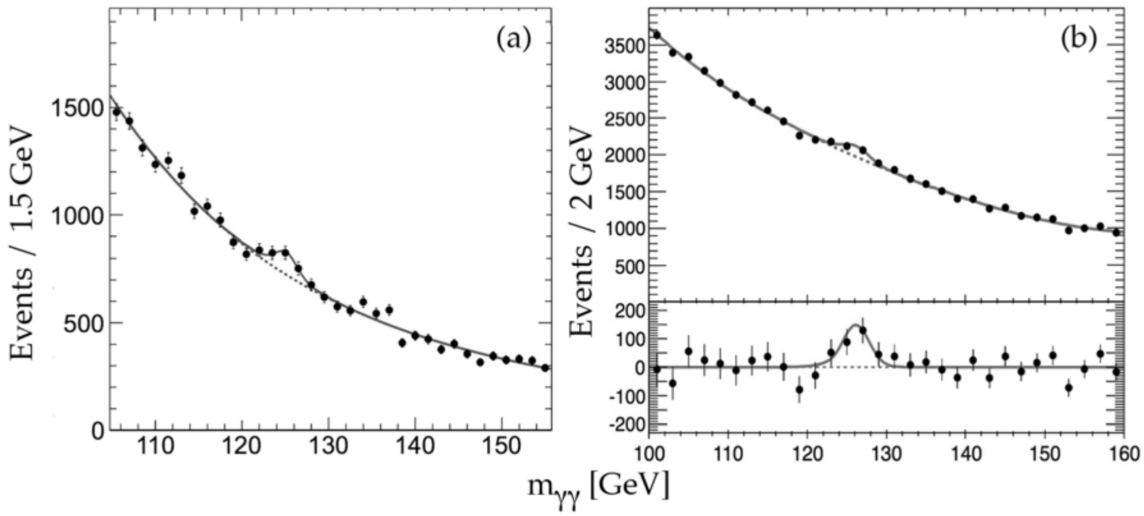

Figure 1.1: *The Higgs candidate observed by CMS (a) and ATLAS (b) in the $\gamma\gamma$ invariant mass distribution.*

We were also involved in the validation and data quality monitoring of τ lepton identification in CMS. Of particular interest is the Higgs decay into a pair of τ leptons, which is expected to have the second largest branching ratio (for a low mass Higgs), with relatively small background (so far the observed excess with respect to background is below 3σ in the 126 GeV mass region). Our group focused in particular on the associated production of a Higgs boson decaying into two τ leptons and a Z^0 or $W^\pm$ boson [3, 4].

Here we report in more details on the analysis results achieved by our group in 2012 on b-physics, heavy baryons and B_s decays which are the subjects of three PhD theses [5, 6, 7] to be presented in 2013. In early 2012 we observed a new usb-baryon (the first new particle observed by CMS before the Higgs discovery) decaying into $\Xi_b^- \pi^+$, followed by $\Xi_b^- \to J/\psi\, \Xi^-$, with $J/\psi \to \mu^+\mu^-$ and $\Xi^- \to \Lambda\pi^-$, $\Lambda \to \pi^- p$. We observed 29 candidates (with a background of 6.6 ± 2.6) and obtained a mass of 5944.9 ± 2.8 MeV. This state is 154 MeV heavier than the spin 1/2 Ξ_b^-. According to theoretical models this would be the Ξ_b^{*0} with spin $\frac{3}{2}$. Details can be found in a recent CMS publication [8] and in our previous (2011) annual report.

1.1 Λ_b polarization in pp collisions

Polarization studies in b-baryon decays provide important information on heavy quark decay dynamics [9]. We have performed a measurement of the Λ_b polarization in pp collisions at 7 TeV using the decay $\Lambda_b \to J/\psi(\to \mu^+\mu^-)\Lambda(\to p\pi^-)$ [5]. From a data sample corresponding to 5 fb^{-1} of integrated luminosity we obtained about 1'800 reconstructed Λ_b and $\bar{\Lambda}_b$ candidates (the $\bar{\Lambda}_b$ decaying into the charge conjugated particles). The $(J/\psi)\Lambda$ invariant mass distribution is shown in fig. 1.2 (left)

The analysis exploits the angular correlations between the daughter particles. The physics parameters (such as polarization and analyzing power) are extracted by a multi-dimensional likelihood fit to the angular distributions. Three angular distributions are employed: $\cos\theta_\Lambda$, $\cos\theta_p$ and $\cos\theta_\mu$, where θ_Λ, θ_p and θ_μ are the polar angles of the Λ, the proton and the μ^+ in the rest frames of Λ_b, Λ and J/ψ, respectively (fig. 1.2, right). The distortions of the angular distributions caused by the geometrical acceptance of the detector and the event selection are determined by Monte Carlo simulation. The contribution from background is determined with data events in the sidebands of the Λ_b mass peak. For a better separation of signal and background the mass distribution is also included in the fit. Note that the polarizations of the Λ_b and $\bar{\Lambda}_b$ are not necessarily equal since their production mechanisms are not identical. Each step of the analysis is therefore performed independently for Λ_b and $\bar{\Lambda}_b$.

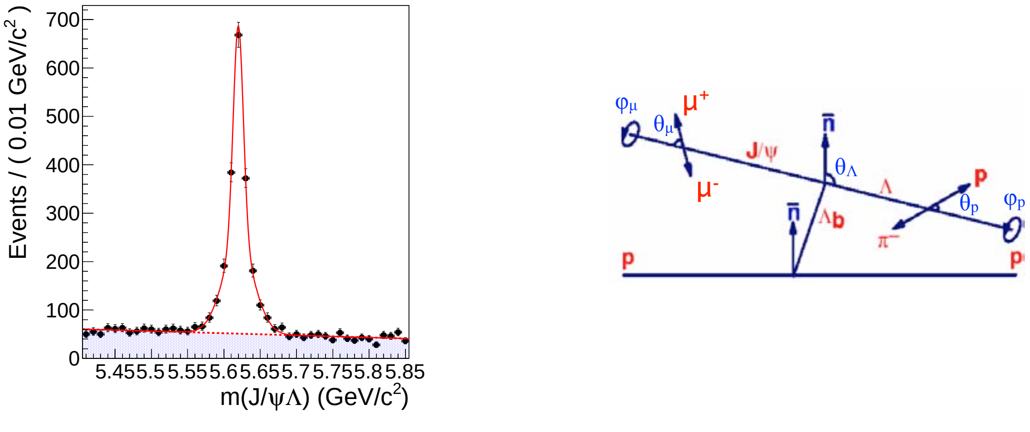

Figure 1.2: *Left:* $(J/\psi)\Lambda$ *invariant mass distribution showing the* Λ_b *(*$\bar{\Lambda}_b$*) with fit (red curve). Right: definitions of the reference frames and angles used in the* Λ_b *polarization analysis.*

Figures 1.3 and 1.4 show the measured angular and mass distributions together with the fits for Λ_b and $\bar{\Lambda}_b$ candidates, respectively. The fit is performed on events within the mass peaks. Our preliminary results show that both Λ_b and $\bar{\Lambda}_b$ are produced with polarizations smaller than 10%. We find for the polarizations of the Λ_b and $\bar{\Lambda}_b$, P_{Λ_b} = 0.03 ± 0.09 ± 0.02 and $P_{\bar{\Lambda}_b}$ = 0.02 ± 0.08 ± 0.05, respectively, where the first uncertainty is statistical and the second systematic. These results are compatible with expectations from perturbative QCD which predict polarization not exceeding 10% in high energy pp collisions [10]. Our results agree with a recent measurement from LHCb which, however, does not distinguish between Λ_b and $\bar{\Lambda}_b$ [11] .

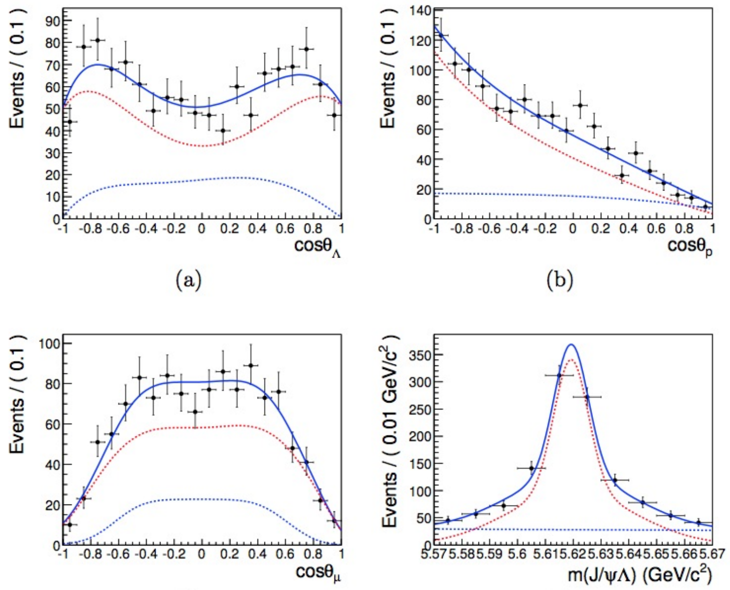

(a) (b)

(c) (d)

Figure 1.3:
a) measured angular distribution of the Λ in the Λ_b rest frame;
b) angular distribution of the proton in the Λ rest frame;
c) angular distribution of the muon in the J/ψ rest frame;
d) mass distribution in the Λ_b region.
The lines show the results from a multi-dimensional likelihood fit: total fit (solid blue), signal folded with efficiency (dashed red) and background contribution (dashed blue).

1.2 Lifetime of the B_s-meson

This analysis [6] focuses on the study and reconstruction of the B_s meson decaying into $(J/\psi)\phi$, where J/ψ decays into two muons of opposite charges, and $\phi(1020)$ into two kaons of opposite charges ($B_s \to J/\psi\ [\to \mu^+\mu^-]\ \phi[\to K^+K^-]$). We are measuring the width difference $\Delta\Gamma_s = \Gamma_L - \Gamma_H$ of the two CP-eigenstates of the B_s-meson, B_L (CP = +1) and B_H (CP = −1). $\Delta\Gamma_s$ is positive [12] and the CP-violating phase ϕ_s is set to zero. This phase has been measured [13], ϕ_s = 0.07± 0.09 [13], and is indeed predicted to be small in the SM, $\phi_s = -0.036 \pm 0.002$.

Since the B_s meson is pseudoscalar and the J/ψ and $\phi(1020)$ are vectors, the orbital angular momentum of the two decay products is L = 0, 1, or 2. For L even we have thus $CP = +1$ (B_L), for L odd $CP = -1$ (B_H). Hence the angular correlations between the decay products are different for the two states [14, 15].

The following cuts are applied to select the $B_s \to (J/\psi)\phi$ candidates. Two muons are required

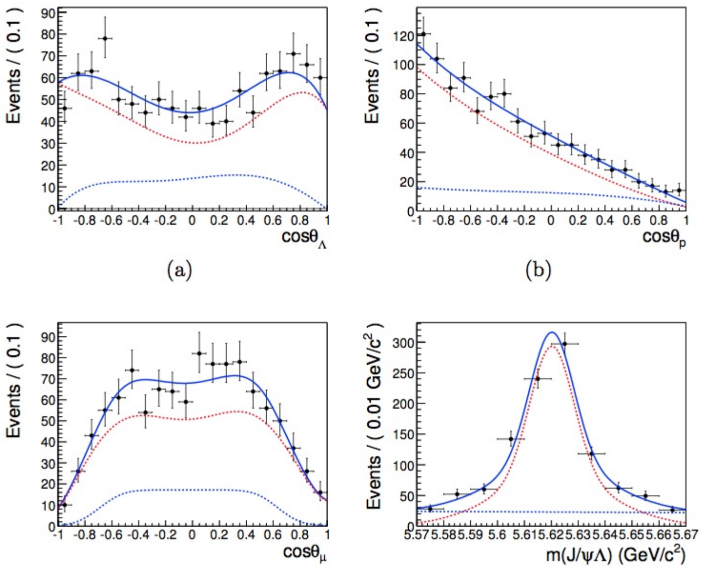

(a) (b)

(c) (d)

Figure 1.4: *(Curves as for fig. 1.3)*
a) measured angular distribution of the of the $\bar{\Lambda}$ in the $\bar{\Lambda}_b$ rest frame;
b) measured angular distribution of the antiproton in the $\bar{\Lambda}$ rest frame;
c) angular distribution of the muon in the J/ψ rest frame;
d) mass distribution in the $\bar{\Lambda}_b$ region.

from a J/ψ candidate emerging from a secondary vertex. The muon pair should have a transverse momentum of at least 7 GeV/c and the mass should lie in a 150 MeV window around the known J/ψ mass. The transverse momentum of the kaon pair is required to be at least 0.7 GeV/c and the invariant mass to lie within 5 MeV of the known $\phi(1020)$ mass. Finally, the B_s candidate invariant mass is required to lie between 5.24 and 5.49 GeV. This leads to 19’200 B_s candidates (fig 1.5, left).

The probability density function (PDF), that describes the decay, includes signal and background contributions. The signal PDF is from a theoretical model that includes the parameters to be fitted [14, 15]. The background PDF is parameterized with an empirical model of the background distributions. A one-dimensional mass fit is performed first on the B_s candidates between 5.24 and 5.49 GeV. The sidebands are then fitted with the empirical model. In the final step the full likelihood fit is performed.

Figure 1.5 shows the fits on the invariant mass distributions (left) and the lifetime distributions (right). Figures 1.6 show the angular distributions. The angles θ and ϕ denote the flight direction (polar and azimuthal angles) of the μ^+ in the J/ψ rest frame. The angle ψ is the polar angle of the K^+ in the rest frame of the $\phi(1020)$ with respect to the negative B_s flight direction [6]. From the 19’200 candidates we find 14’310 ± 138 B_s events, leading to a mean mass of 5366.8 ± 0.1 MeV [16]. We also obtain

$$\Delta\Gamma_s = 0.048 \pm 0.024\ \text{(stat.)} \pm 0.003\ \text{(syst.)}\ \text{ps}^{-1}, \tag{1.1}$$

$$\tau_{B_s} = 1.528 \pm 0.020\ \text{(stat.)} \pm 0.010\ \text{(syst.)}\ \text{ps}. \tag{1.2}$$

Our measurements are compared with the ATLAS and LHCb results in Table 1.1 (errors added in quadrature). The LHC results are in good agreement with predictions from the SM.

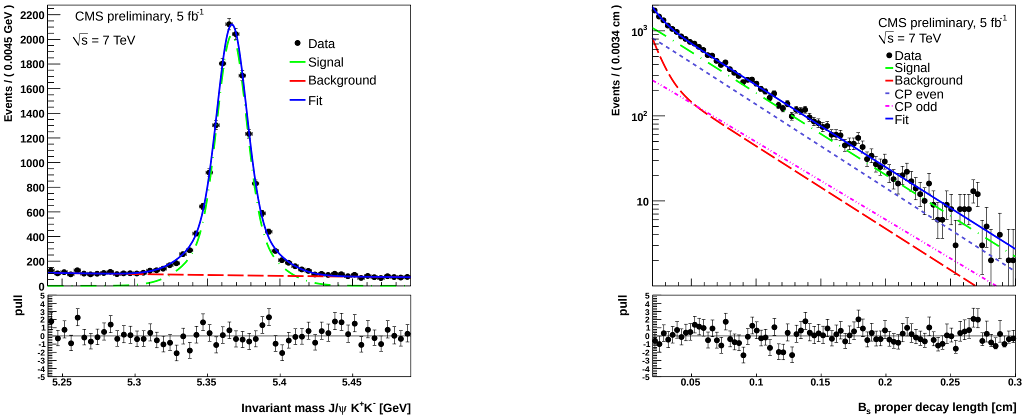

Figure 1.5: *Left: Invariant mass distribution of the B_s candidates. The black points are the data. The blue line describes the five-dimensional maximum likelihood fit, the green line is the signal and the red line the background contribution. Right: Projection of the proper decay length from the 5D maximum likelihood fit. The solid blue line is the fit, the green line the signal, the red line the background. The magenta dashed line shows the CP odd component, the purple dashed line the CP even component.*

	Γ_s [ps^{-1}]	$\Delta\Gamma_s$ [ps^{-1}]
CMS [16]	0.655 ± 0.010	0.048 ± 0.024
ATLAS [17]	0.677 ± 0.008	0.053 ± 0.023
LHCb [13]	0.663 ± 0.008	0.100 ± 0.017

Table 1.1: *Measurements of Γ_s and $\Delta\Gamma_s$ from the decay $B_s \rightarrow (J/\psi)\phi$ at the LHC. The SM prediction is $\Delta\Gamma_s$ = (0.147 ± 0.060) × Γ_s = 0.097 ± 0.039 ps^{-1}.*

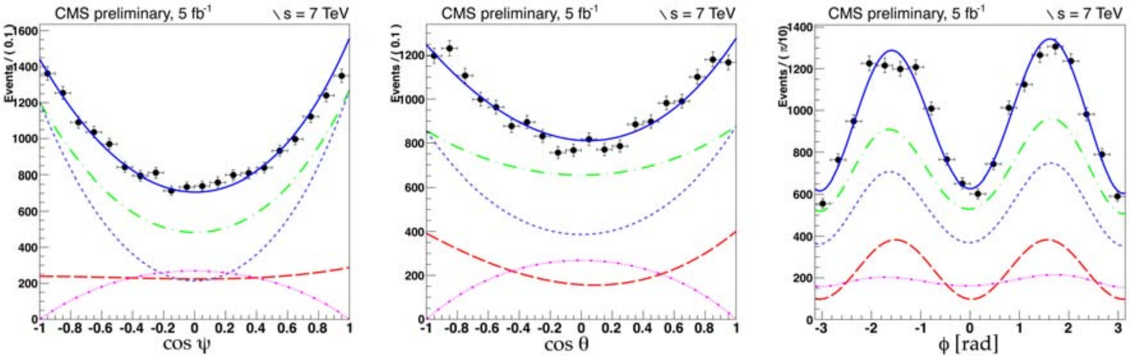

Figure 1.6: *Angular distributions of* $\cos\psi$, $\cos\theta$ *and* ϕ *(see text). The solid blue lines are the fit, the green lines the signal component, the red lines the background component. The magenta dashed line are the CP odd component, the purple dashed line the CP even component.*

1.3 Angular correlations of b hadrons associated with Z^0 bosons

The production of b-quark pairs associated with Z^0 bosons is the main background in Higgs decays into $b\bar{b}$ pairs (this decay channel having the largest branching fraction for a low mass Higgs). The validation of calculation techniques to estimate correctly the background in Higgs searches is therefore important.

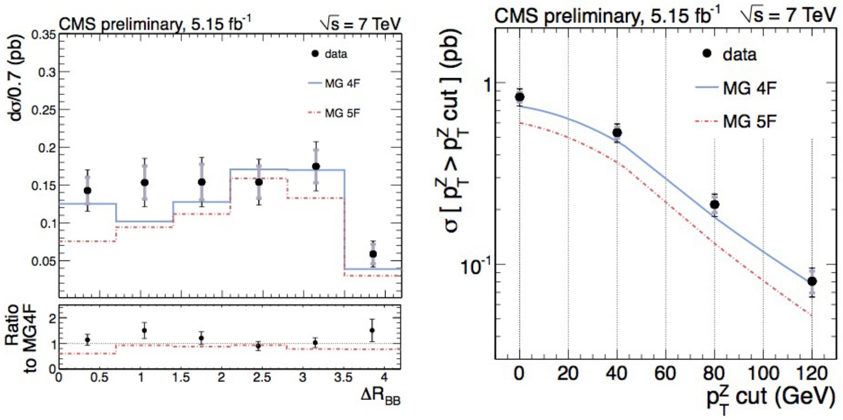

Figure 1.7: *Left: Differential cross section for pp* $\rightarrow Z^0 b\bar{b} + X$ *as a function of* ΔR_{BB}*. The data are represented by the black circles, the MADGRAPH MC predictions are shown as histograms. Right: Total production cross section vs. minimal* p_T *of the* Z^0 *boson.*

We performed a measurement of the total cross section and of the angular correlations between b hadrons produced in association with Z^0 bosons decaying into two leptons (muons or electrons) [7, 18]. The b and $\bar{b}$ hadrons were identified through their relatively long lifetime leading to secondary decay vertices. The three-dimensional angular separation between the b and $\bar{b}$ hadrons is denoted as ΔR_{BB}.The differential cross section as a function of ΔR_{BB} and the total cross section for different Z^0 transverse momenta p_T are shown in fig. 1.7. The measurements are compared to the tree-level predictions by MADGRAPH MC, in the four- and five-flavour calculation schemes. Our measurement show that the four-flavour predictions in MADGRAPH provide the best description of data.

References

[1] CMS Collaboration, Phys. Lett. **B 716** (2012) 30;
ATLAS Collaboration Phys. Lett. **B 716** (2012) 1
[2] C. P. Buszello *et al.*, Eur. Phys. J. **C32** (2004) 209; S.Y. Choi *et al.*, Phys. Lett. **B 553** (2003) 61
[3] CMS Collaboration, CMS-PAS-HIG-12-053
[4] M. Verzetti, PhD-thesis, Universität Zürich (in preparation)
[5] M. Ivova Rikova, PhD-thesis, Universität Zürich (Submission in June 2013)
[6] B. Millán Mejías, PhD-thesis, Universität Zürich (Submission in June 2013)
[7] C. Favaro, PhD-thesis, Universität Zürich (in preparation)
[8] CMS Collaboration, Phys. Rev. Lett. **108** (2012) 252002
[9] M. Krämer and H. Simma, Nucl. Phys. **B 50** (1996) 125
[10] G. Hiller *et al.*, Phys. Lett. **B 649** (2007) 152
[11] LHCb Collaboration, arXiv:1302.5578 (2013)
[12] LHCb Collaboration, Phys. Rev. Lett. **108** (2012) 241801
[13] LHCb Collaboration, arXiv:1304.2600 (2013)
[14] A.S. Dighe, I. Dunietz and R. Fleischer, Eur. Phys. J. **C 6** (1999) 647
[15] I. Dunietz, R. Fleischer and U. Nierste, Phys. Rev. **D63** (2001) 114015
[16] CMS Collaboration, CMS PAS BPH-11-006, http://cds.cern.ch/record/1484686?ln=en
[17] ATLAS Collaboration, arXiv: 1208.0572 (2013)
[18] CMS Collaboration, CMS-PAS-EWK-11-015

2 Liquid argon scintillation from neutron induced recoils

C. Amsler, W. Creus, A. Ferella, C. Regenfus, and J. Rochet

Weak Interacting Massive Particles (WIMPs) are prime candidates for dark matter. The interaction of WIMPs in detectors (e.g. noble liquids such as liquid argon, LAr) leads to nuclear recoils generating scintillation light. A low energy detection threshold of a few keV is required. However, at such low energies the response of LAr is poorly known, light quenching being expected for highly ionizing particles. The determination of the scintillation efficiency $\mathcal{L}_{\text{eff}}$ relative to that for minimum ionizing particles (such as electrons) is therefore crucial. This can be conveniently investigated with neutron scattering in argon. To achieve this goal we have built a neutron scattering facility in our laboratory at CERN.

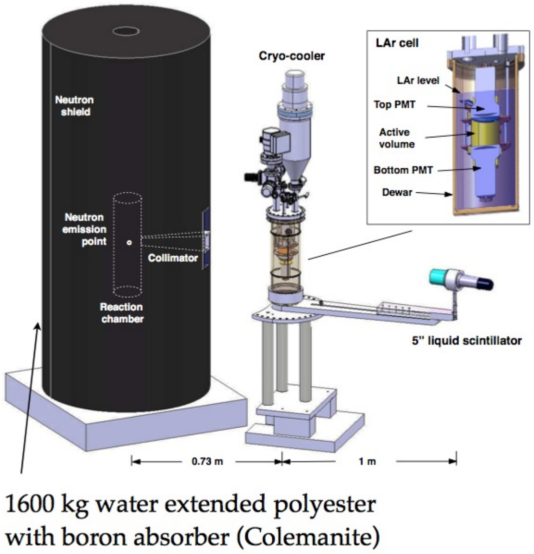

Figure 2.8: *Neutron generator, LAr target and neutron detector. Insert: LAr target cell.*

Monochromatic neutrons of 2.45 MeV are produced by a dd fusion generator (from NSD-Fusion) and induce nuclear recoils in the LAr cell (fig. 2.8). Our generator delivers up to $2{\cdot}10^6$ isotropically emitted mono-energetic neutrons from the two-body reaction $dd \rightarrow {}^3\text{He} + n$. The reaction chamber is surrounded by a 1.6 t polyester cylinder with 2 mm Pb cladding, keeping an acceptable radiation dose from neutrons and X-rays. The structure of the cryogenic cell in shown in the insert of fig. 2.8. The detector consists of two Hamamatsu R6091-01 photomultipliers (PMT) separated by 47 mm and forming a cylindrical sensitive volume of $0.2\ \ell$. The PMTs were coated with a TPB (tetra-phenyl-butadiene/paraloid) mixture to convert the 128 nm light to $\sim$ 420 nm. The cylinder containing the LAr was covered with a Tetratex/TPB reflector.

The scattered neutrons in the LAr cell are detected by an organic liquid scintillator at a given scattering angle θ which defines the energy of the recoiling argon nucleus. Neutron tagging is performed via pulse shape discrimination on the scintillation light, the organic liquid scintillator being capable of distinguishing nuclear recoils form electron recoils. In addition, the neutron time of flight is recorded to reduce background, mainly from inelastic collisions.

Liquid argon generates fast and slow light with decay times of $\tau_1 \simeq 6$ ns (from the excimer singlet state) and $\tau_2 \simeq 1.6\ \mu$s (from the triplet state). Above 10 keV (electron equivalent) heavily ionizing particles feed mostly the fast component, while electrons contribute mostly to the slow component [1]. Impurities in LAr (such as N_2, O_2, H_2O and $CO + CO_2$) can quench argon excimers or absorb the VUV scintillation light. This decreases τ_2, inducing losses in the slow scintillation light [2].

In 2012 we developed a new technique to correct for the reduced light caused by argon impurities. This method consists in dividing the pulse shape in three regions I1, I2, and L, as illustrated in fig.2.9 (left). The first part (I1) corresponds to $4\tau_1$. The integral over I1 contains the contribution from A (singlet excimer state), the contribution of C (intermediate state [2]) and B (triplet excimer state). The intermediate state C is taken into account by integrating the signal over a time window between 40 ns and 100 ns (I2, containing also part of B). The rest of the pulse shape L is divided logarithmically in five time bins from t_0 to t_5. The population density of the triplet state between t_0 and t_5 is obtained from the weighted mean of the integrals, times the number of bins. Details can be found in ref. [3].

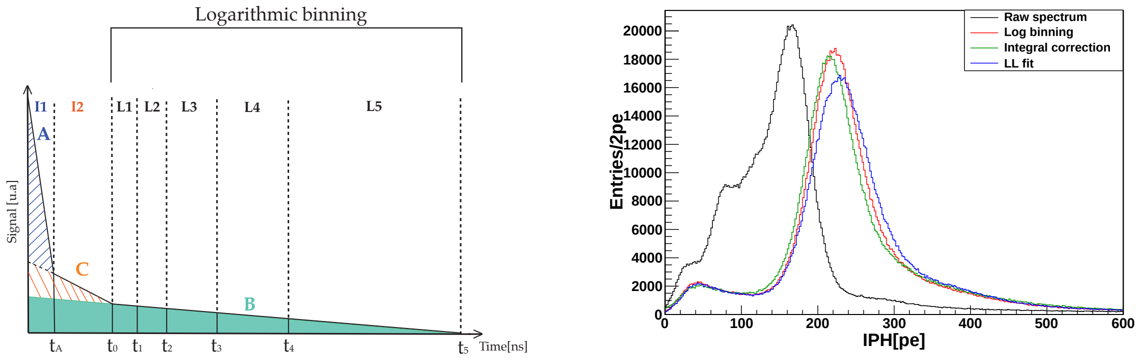

Figure 2.9: *Left: logarithmic binning method showing the contributions of the populations A, B and C. Right: pulse height distribution (in photoelectrons, p.e.) for the incorrected fit (black curve) and various reconstruction methods using the log binning method (colored curves).*

Fig. 2.9 (right) shows the raw energy distribution from a ^{241}Am radioactive source (60 keV-γ) for runs taken under various purity levels. Mixing data with different purities leads to a spread of the deposited energy distribution (black curve). However, applying the log binning method to correct the spectrum leads to a dramatic decrease of the width of the distribution, also shifting the distribution to higher numbers of photoelectrons (p.e.), in average 3.9 p.e./keV electron equivalent.

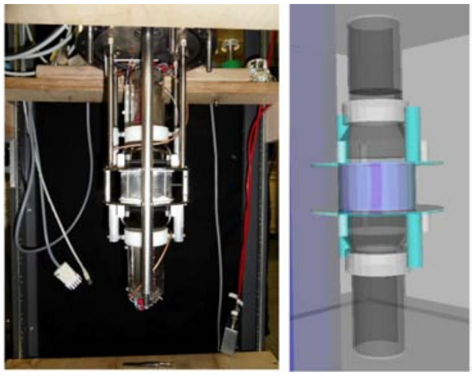

Figure 2.10: *Left: picture of the LAr cell. Right: GEANT4 material model.*

A detailed GEANT4 simulation was written for the neutron experiment. Several components were included in the simulation to give a faithful description of the apparatus: The simulation takes into account the assembly of the neutron generator with its shielding and collimator. Also the vacuum cryostat and different components of the LAr detector (vessel, reflector foil, PMTs, support frame, etc.) and the liquid scintillators are implemented in the simulation. A photograph of the LAr cell is shown in fig.2.10 with a drawing of the simulated cell for comparison.

Neutrons of 2.45 MeV were generated isotropically in 4π and 10^8 events produced for each scattering angle. Neutrons loose energy by elastic scattering, inelastic scattering (nuclear excitation), multiple elastic scattering, and external scattering (outside the fiducial volume). Fig.2.11 (left) shows as an example the various contributions to the recoil energy distribution for a scattering angle of 40° (28.5 keV nuclear recoil). A time of flight cut between 41 and 48 ns was applied. The energy spectrum contains a clear elastic peak corresponding to the expected energy deposit, over an exponentially decreasing background. Neutrons that elastically scatter once in LAr before being detected by the liquid scintillator (58%) are represented by the blue histogram. The dashed red histogram includes neutrons that scatter elsewhere before and/or after the interaction with argon (33%). Multiple scattering, illustrated in green, is low (9.4%) due to the small dimension of the LAr cell. The contribution from inelastic neutron scattering is negligible. Fig.2.11 (right) shows the finally measured pulse height distribution.

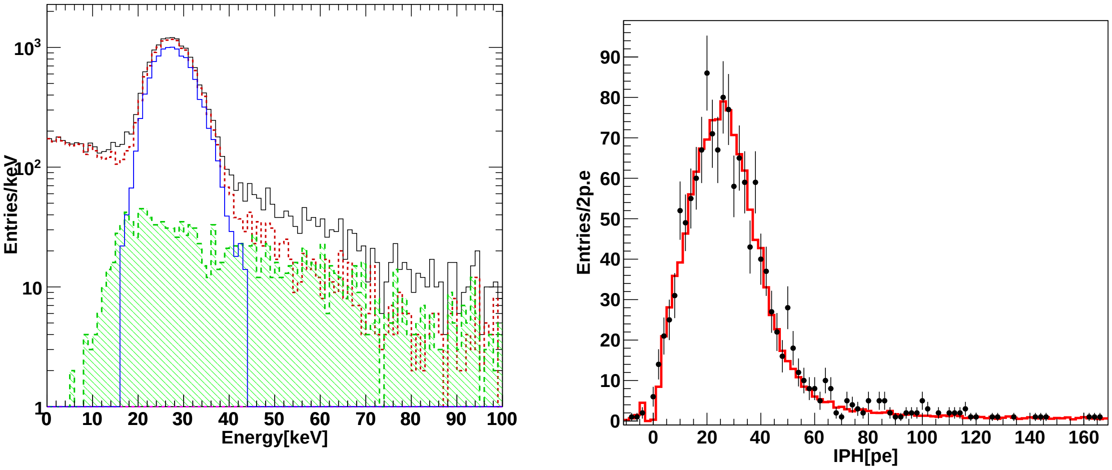

Figure 2.11: *Left: simulated spectrum at $\theta = 40^\circ$ after the time of flight cut (see text). Right: measured pulse height distribution at 40° and best fit of the simulated recoil spectrum (red histogram).*

A χ^2 minimization between the measured and the simulated distributions is then performed. To obtain the simulated spectrum in photoelectrons, the values of the deposited energy (in keV, nuclear recoil) are first multiplied by the light yield $\mathcal{L}_{\text{eff}}$ (first free fitting parameter). We use a Poisson function for the number of photoelectrons and a Gauss function for the energy resolution (second free parameter). Fig. 2.11 (right) shows the measured nuclear recoil spectrum at 40°. The best fit is illustrated by the superimposed red histogram and is obtained for $\mathcal{L}_{\text{eff}} = 0.289 \pm 0.012$.

Finally, we show in Table 2.2 and in fig. 2.12 our results for the light yield $\mathcal{L}_{\text{eff}}$, as a function of scattering angle. These values update the preliminary results reported in ref. [1].

θ [°]	Recoil energy [keV]	$\mathcal{L}_{\rm eff}$
25	11.4	0.386 ± 0.033
30	16.4	0.305 ± 0.021
40	28.5	0.289± 0.012
50	43.4	0.294 ± 0.024
60	60.5	0.283 ± 0.020
90	119.5	0.301 ± 0.021

Table 2.2: *Results for $\mathcal{L}_{\rm eff}$ from argon recoils (relative to electrons) vs. scattering angle θ.*

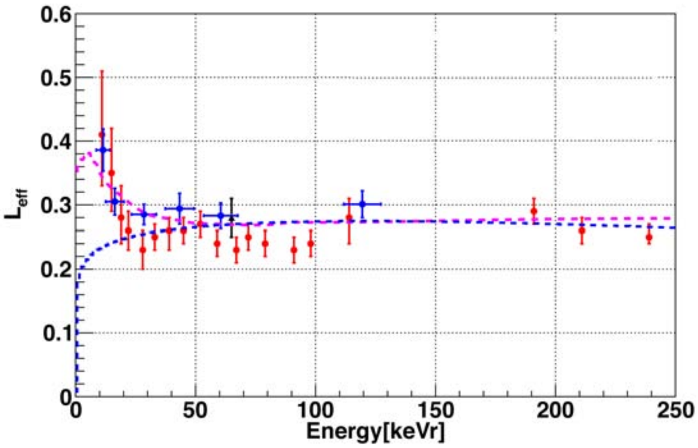

Figure 2.12: *$\mathcal{L}_{\rm eff}$ vs. recoil energy. The blue data points are from this work [3], the red points from micro-Clean [4] and the black point from WARP [5]. The blue and pink dashed lines are theoretical predictions from the Mei [6] and the NEST [7] models, respectively.*

References

[1] C. Regenfus *et al.*, Journal of Physics: Conference Series **375** (2012) 012019, arXiV:1203.0849
[2] V. Boccone *et al.*, J. of Instrumentation **4** (2009) P06001
C. Amsler et al., J. of Instrumentation **5** (2010) P11003
[3] W. Creus, PhD-thesis, Universität Zürich (Submission in June 2013)
[4] D. Gastler *et al.*, Phys. Rev. **C 85** (2012) 065811
[5] R. Brunetti *et al.*, New Ast. Rev. **49** (2005) 265
[6] D.–M. Mei *et al.*, Astropart. Phys. **30** (2008)12
[7] M. Szydagis *et al.*, arXiv: 1106.1613

3 Test ot the equivalence principle with antihydrogen

C. Amsler[1,2], A. Ariga[2], T. Ariga[2], C. Canali[1], A. Ereditato[2], L. Jørgensen[1], J. Kawada[2], M. Kimura[1,2], C. Pistillo[2], C. Regenfus[1], J. Rochet[1], P. Scampoli[2,3], and J. Storey[1,2]

and the AEgIS Collaboration.

[1] Physics Institute, University of Zurich, Switzerland
[2] Albert Einstein Center for Fundamental Physics, Laboratory for High Energy Physics, University of Bern, Switzerland
[3] Department of Physics, University of Napoli Federico II, Napoli, Italy

The main goal of the AEgIS experiment (CERN/AD6) is to test the Weak Equivalence Principle (WEP) using antihydrogen ($\bar{H}$). This principle of the universality of free fall has been tested with high precision for matter, but not with antimatter, due to major technical difficulties related to stray electric and magnetic fields. In contrast, the electrically neutral $\bar{H}$ atom is an ideal probe to test the WEP, and the antiproton decelerator (AD) at CERN is a worldwide unique antihydrogen factory. In AEgIS the gravitational deflection of $\bar{H}$ atoms launched horizontally and traversing a moiré deflectometer will be measured with an initial precision of 1% on $|\Delta g|/g$, using a position sensitive annihilation detector. Details on the experiment can be found in ref. [1, 2]. In the original proposal [1] a resolution of some 10 μm was to be achieved with a silicon strip annihilation detector.

In 2012 we tested a new idea to instead use emulsion films to achieve a resolution of the order of 1 μm [3, 4], and completed the construction of the annihilation detector (FACT) to characterize the antihydrogen cloud prior to its acceleration into an $\bar{H}$ beam. Most of the AEgIS apparatus (apart from the gravity section) was also commissioned in 2012, including the antiproton capture trap and the positron line. A photograph of the apparatus is shown in fig. 3.13.

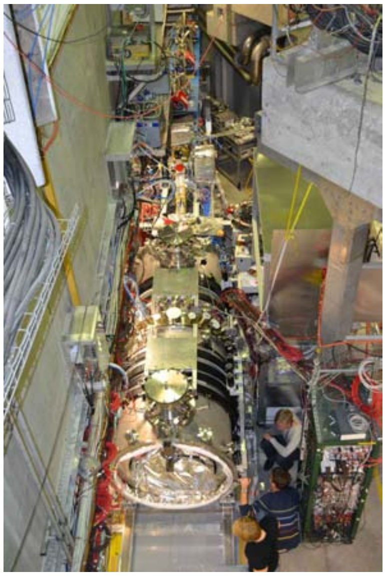

Figure 3.13: *Picture of the AEgIS apparatus in the AD-hall at CERN in December 2012.*

3.1 Nuclear emulsions to measure g with antihydrogen

Nuclear emulsions [5] are photographic films with extremely high spatial resolution. A track produced by a charged particle is detected as a sequence of silver grains, where about 36 Ag grains per 100 μm are created by a minimum ionizing particle. The intrinsic spatial resolution is around 50 nm.

For AEgIS we developed nuclear emulsions which can be used in ordinary vacuum (OVC, 10^{-5} – 10^{-7} mbar). Fig. 3.14 (left) shows the setup envisaged for the g-measurement. The expected performance is also shown: The number of antihydrogen annihilations required to achieve a given precision decreases dramatically with improving resolution.

A sketch of the setup used for test exposures with stopping antiprotons in 2012 is shown in fig. 3.14 (right). The emulsion detector consisted of 5 sandwiches made of emulsion films (OPERA type) deposited on both sides of (200 μm thick) plastic substrates (68 x 68 x 0.3 mm^3). A thin foil will be needed in the g-measurement as a window to separate the $\bar{H}$ beam line at UHV pressure from the OVC section containing the emulsion detector. Thus for the tests half of the emulsion surface was covered by a 20 μm (SUS) stainless steel foil, while direct annihilation on the emulsion surface could be investigated from the other half.

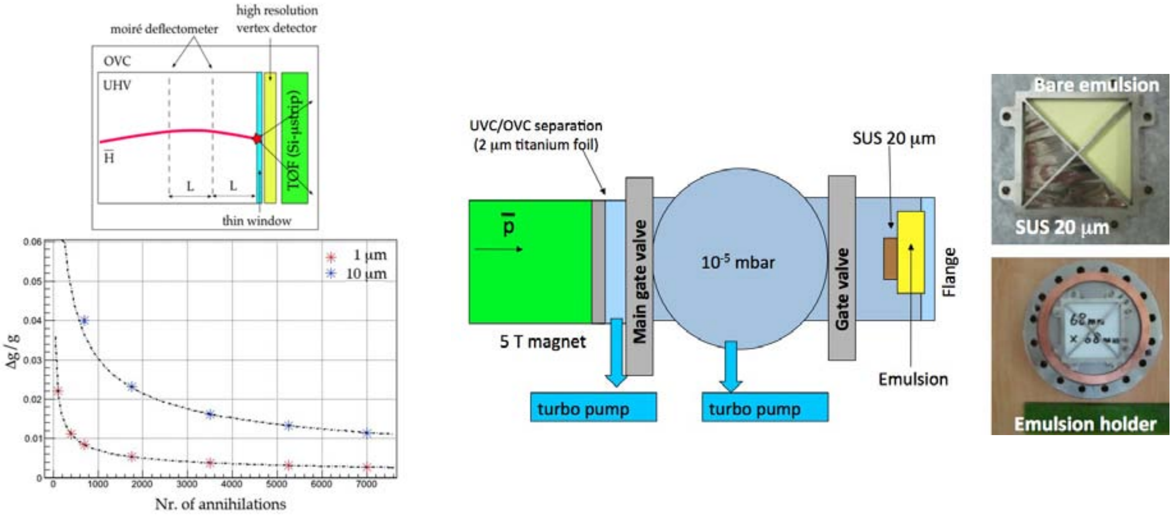

Figure 3.14: *Left: schematics of the AEgIS detectors. The vertex detector is made of nuclear emulsions. The time-of-flight detector (TOF) is needed to measure the velocities of the* $\bar{H}$ *atoms. Bottom:* $\Delta g/g$ *vs. number of particles for a vertex resolution of 1* μm *(red) and 10* μm *(blue). Right: test setup with a picture of the vacuum flange holding the emulsion stack attached by a crossed bar frame.*

In December 2012 we also carried out measurements with a series of thin foils of varying compositions (Al, Si, Ti, Cu, Ag, Au, Pb) to determine the relative contributions from protons, nuclear fragments and pions as a function of atomic number. Fig. 3.15 (left) shows annihilation vertices on the bare emulsion surfaces and tracks behind a 5 μm thick silver foil. Tracks emerging from the annihilation vertex are clearly observed. Tracks from nuclear fragments, protons, and pions were reconstructed and the distance of closest approach between pairs of tracks was calculated. Fig. 3.15 (right) shows the distribution of the distance of closest approach projected into the vertical direction (impact parameter), which is a measure of the resolution with which the annihilation point will be determined in the g-measurement. The figure shows that with *e.g.* a 20 μm steel window a resolution of $\simeq 1$ μm on the vertical position of the annihilation vertex can be achieved.

We have tested the properties of nuclear emulsions in vacuum [3] which, to our knowledge, had not been studied before. Water loss in the gelatine which surrounds the AgBr crystals produces cracks in the emulsion layer, thus compromising the mechanical stability (required at the μm level). We therefore developed a treatment with glycerine to prevent the elasticity loss in the emulsion. However, glycerine treatment changes the composition of the emulsion layer and we thus had to determine the

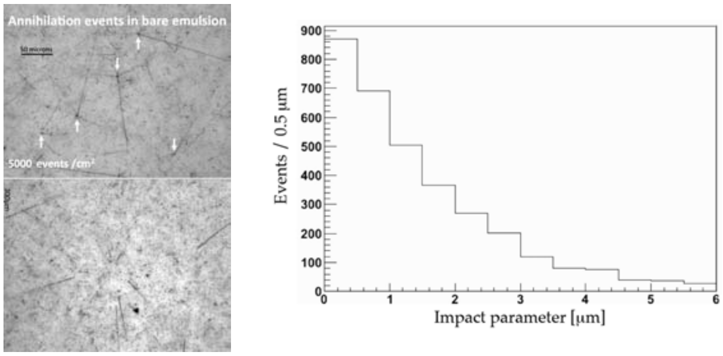

Figure 3.15: *Left: typical antiproton annihilation vertices in the bare emulsion (top) and tracks observed behind a thin silver foil in which the antiprotons annihilate (bottom). Right: impact parameter resolution with a 20 μm stainless steel window.*

detection efficiency per AgBr crystal. This was performed with minimum ionizing pions in a 6 GeV/c CERN beam. The result (fig. 3.16) does not indicate any changes in the efficiency, which is typically 13% for glycerine concentrations below 20%. However, the thermally induced background – the so-called fog density – increases for glycerine treated emulsions.

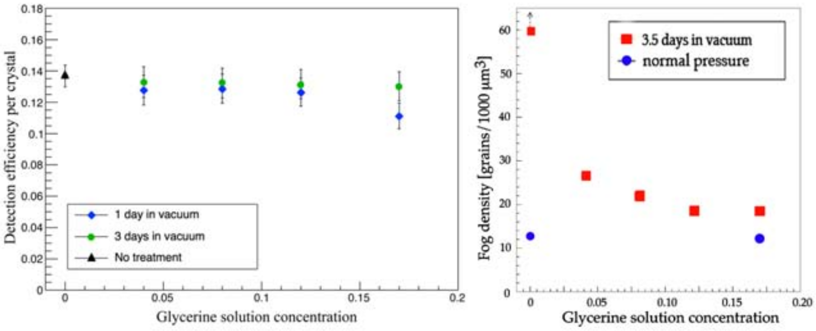

Figure 3.16: *Left: Crystal sensitivity vs. glycerine concentration. Right: Fog density (number of noise grains per 10^3 μm^3) vs. glycerine concentration for films kept in vacuum for 3.5 days (squares), compared films kept at atmospheric pressure (dots).*

Annihilation products from annihilating antiprotons (or $\bar{H}$ atoms) are emitted isotropically, in contrast to the τ-decay products measured in the OPERA experiment, which are forward boosted. The efficiency of the automatic scanning system available in Bern needs therefore to be improved for tracks traversing the emulsion layers at large incident angles. We are also investigating new emulsion gels with higher sensitivity to increase the detection efficiency for minimum ionizing particles. They were developed at Nagoya University (Japan) and coated onto glass substrates in Bern. Glass is well suited for highest position resolutions thanks to its superior environmental stability (temperature and humidity), as compared to plastic.

A proof of principle of the deflectometer to be used AEgIS was also performed in 2012 with emulsion films irradiated with antiprotons passing through a small moiré deflectometer. A photograph of the deflectometer is shown in fig. 3.17 (left). The device contained several pairs of gratings with different spacings, as well as gratings in direct contact with the films. The simulation in fig. 3.17 (right) shows as an example the expected interference pattern at the emulsion layer, generated by a pair of gratings (12 μm slit, 40 μm pitch, separated by L = 25 mm). The antiproton data is being analyzed and preliminary results are quite encouraging.

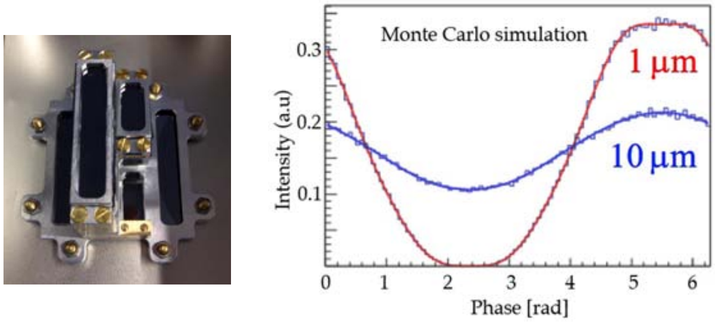

Figure 3.17: *Left: photograph of miniature moiré deflectometer. Right: simulated intensity distribution of reconstructed vertices with position resolutions of 1 µm (red) and 10 µm (blue).*

3.2 Fast Annihilation Cryogenic Tracking detector (FACT)

The FACT detector [6] will measure the production and temperature of the $\bar{H}$ atoms. The operating requirements for this detector are challenging as it needs to identify each of the ~thousand annihilations in the 1 ms interval of pulsed $\bar{H}$ production, operate at 4 K inside a 1 T solenoidal field, and produce less than 10 W of heat. A schematic of the detector is shown in fig. 3.18 (left). The detector consists of two concentric cylindrical layers of scintillating fibers. The scintillating fibers are coupled to clear fibers which transport the scintillation light to 800 silicon photomultipliers. Each silicon photomultiplier signal is connected to an amplifier and a fast discriminator, the outputs of which are sampled continuously by Field Programmable Gate Arrays (FPGAs). The detector is optimised to reconstruct the position of the annihilation vertex along the beam axis, knowledge of which will enable measurements of antihydrogen production, temperature and beam creation. From GEANT4 simulations an annihilation vertex resolution of $\sigma = 2.1$ mm is expected, which is sufficient for the AEgIS requirements.

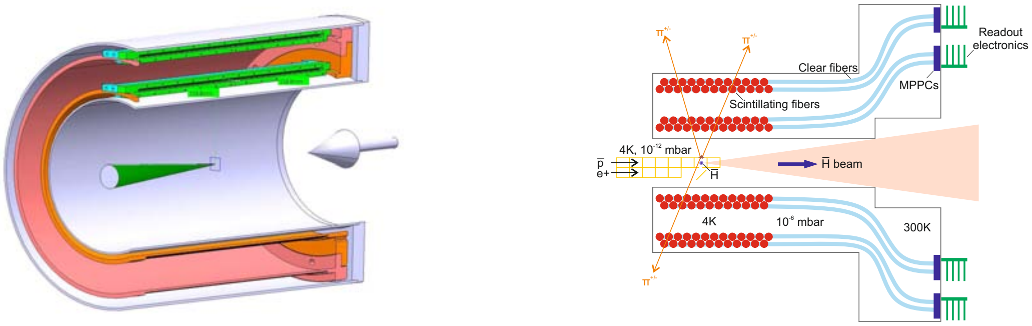

Figure 3.18: *Left: section view of the support structure of the FACT detector. The beam axis is indicated by the arrow and the green cone illustrates the $\bar{H}$ beam region. Right: layout of the detector (see text).*

The two scintillating fiber layers are mounted on 240 mm long cylindrical support structures (orange and pink cylinders in fig. 3.18). The fibers are located in U shaped grooves. The blue and green bars are the connectors to couple the scintillating and clear fibers. The scintillating fibers are arranged in loops aligned orthogonally to the beam axis. There are 2 layers at radial distances of 70 mm and 98 mm from the beam axis. Each layer consists of 400 scintillating fibers (1 mm diameter Kuraray SCSF-78M) separated by 0.6 mm, with alternate fibers displaced radially by 0.8 mm. The scintillating light is transported from the cryogenic region to the room temperature readout electronics by means of 2 m long clear fibers (fig. 3.18, right). Particular attention is given to the routing of the clear fibers to ensure that the minimum bending radius always exceeds 50 mm to avoid light losses. Charged pions (orange lines) from annihilations are reconstructed using the scintillating fiber tracker and extrapolated back to the $\bar{H}$ formation region to identify the annihilation vertex (r, z - coordinates). Fig.

3.19 shows the the fibers before (left) and after (middle) being mounted on the support structure.

The scintillation light is guided onto a Hamamatsu Multi-Pixel Photon Counter (MPPC) consisting of 100 Geiger mode Avalanche Photo Diodes (APDs), operating in parallel with a total photosensitive area of 1 mm^2. The readout electronics is designed to detect continuously the light from the scintillating fibers for the duration of the 100 ms period during which $\bar{H}$ is produced. The MPPC signal is connected to an amplifier and a fast discriminator read directly by a FPGA. To minimise the heat load to the cryogenic region only the MPPCs are placed inside the vacuum vessel. A plastic connector (developed by the T2K collaboration) is used to couple the clear fibers to the MPPC. The identity of every clear fiber is labelled with coloured glass beads. A photograph of an assembled vacuum feedthrough is shown in fig. 3.19 (right).

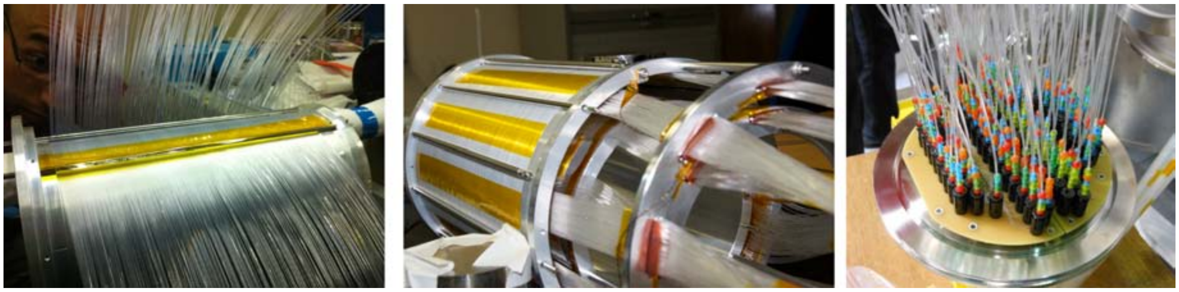

Figure 3.19: *Left and middle: scintillating fibers before and after being mounted on the support structure. The clear fibers emerging form the support structure are organised into groups of 25 fibers and fixed into a circular plate with rectangular slots. Right: clear fibers connected to the MPPCs.*

Fig. 3.20 shows a photograph of the readout electronics. The signals from 96 MPPCs on the vacuum side are routed via the backplane PCB to one of four analogue boards. The readout is supervised by a Xilinx Spartan-6 FPGA development board (bottom left corner). The complete readout system consists of 9 vacuum feedthroughs, 18 backplane PCBs, 67 analogue boards and 16 Spartan-6 development boards.

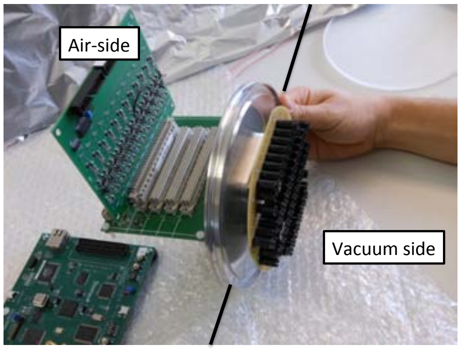

Figure 3.20: *Air and vacuum side electronics for the FACT detector (see text).*

Tests of the plastic scintillating fibers at 4 K have been performed to study the light yield, the decay time and the lifetime of the fibers at cryogenic temperatures. The apparatus to perform this measurement consisted of 3 layers of 1 mm diameter scintillating fibers arranged in loops at the bottom of a liquid helium cryostat. The performance of the scintillating fibers was monitored using cosmic rays. The rate of events as a function of temperature decreased by $\approx 10\%$ from room to liquid helium temperature. Examination of the fibers under a microscope after many cycles to 4 K revealed no sign of mechanical damage.

The FACT detector was installed in the AEgIS apparatus in 2012 and is currently undergoing commissioning with cosmic-rays. FACT will be used to study $\bar{H}$ formation, when the low energy antiproton physics programme resumes at CERN in 2014.

References

[1] G. Drobychev *et al.*, http://doc.cern.ch/archive/electronic/cern/preprints/spsc/public/spsc-2007-017.pdf;

[2] A. Kellerbauer *et al.*, Nucl. Instr. and Meth. **B 266** (2008) 351

[3] C. Amsler *et al.*, J. of Instrumentation **8** (2013) P02015

[4] M. Kimura *et al.*, 13th Vienna Conference on Instrumentation, Vienna (2013)

[5] G. de Lellis, A. Ereditato, K. Niwa, *Nuclear Emulsions*, C. W. Fabjan and H. Schopper eds., Springer Materials, Landolt-Börnstein Database (http://www.springermaterials.com), Springer-Verlag, Heidelberg, 2011

[6] J. Storey *et al.*, 13th Vienna Conference on Instrumentation, Vienna (2013)

4 Study of πK atoms

C. Amsler, A. Benelli, and J. Rochet

and the DIRAC Collaboration.

The main initial goal of the DIRAC experiment was to study $\pi^+\pi^-$ atoms (pionium) and to measure the $\pi\pi$ scattering lengths a_0 and a_2 (isospins 0 and 2). Final results for $\pi^+\pi^-$ have been published [1]. The difference in the scattering lengths was measured, $|a_0 - a_2|$ = 0.2533 ± 0.0109 m_π^{-1} from 21'227 $\pi^+\pi^-$ atomic pairs. This corresponds to a mean life of 3.15 ± 0.28 fs. Detailed news from the DIRAC experiment can be found in ref. [2].

We joined the DIRAC collaboration in 2007 to search for πK atoms and to measure the πK scattering lengths $a_{1/2}$ and $a_{3/2}$ (isospins 1/2 and 3/2). An artist's view of the DIRAC spectrometer and a photograph of the experiment in the CERN-PS-South Hall is shown in fig. 4.21. The 24 GeV/c proton beam passes through a thin target (such as 100 μm Ni). The secondary particles traverse a scintillation fiber detector (SFD). The secondary hadrons produced in target are analyzed in a double-arm magnetic spectrometer measuring the momentum vectors of two oppositely charged hadrons. Positive particles are deflected into the left arm, negative ones into the right arm. The spectrometer is slightly tilted upwards with respect to the proton beam. Electrons and positrons are vetoed by N_2-Čerenkov detectors (N) and muons by their signals in scintillation counters (Mu) behind steel absorbers. The preshower detector (PSh) provides an additional electron/hadron separation to the N_2-Čerenkov. Details can be found in previous annual reports and in ref. [3].

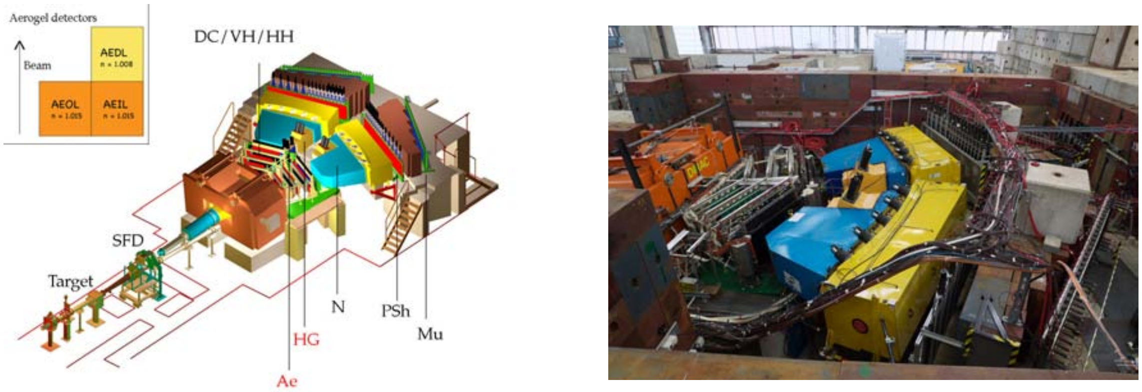

Figure 4.21: *Left: DIRAC spectrometer: SFD = scintillator fibre detector, DC = drift chambers, VH, HH = vertical and horizontal scintillation hodoscopes, PSh = preshower, Mu = muon counters, Ae = aerogel, HG = heavy gas and N = N_2-Čerenkov counters. The inset shows the arrangement of the three aerogel modules. Right: photograph of the apparatus.*

In 2007 we modified the DIRAC setup to study πK atoms while at the same time collecting more data for $\pi\pi$ atoms. In both arms the N_2-Čerenkov counters were cut to leave space for heavy gas (C_4 F_{10}) Cerenkov detectors (HG). They identify pions with an efficiency of more than 99% while not responding to kaons nor to (anti)protons. On the left side we installed an aerogel Čerenkov detector (Ae) to identify kaons and reject protons. The detector consists of two modules with refractive index 1.015 and one module with refractive index 1.008 to cover the high momentum range of kaons between 5.5 and 8 GeV/c. Our group has developed and built the 37ℓ aerogel Čerenkov counter [4] and the gas system for the C_4F_{10} counters [5].

Using only the downstream part of DIRAC for tracking we published the first evidence for πK

atoms [6, 7]. The signal (173 ± 54 events) was observed for πK-pairs with very small relative momenta (typically $|Q_L| < 3$ MeV/c is the c.m.s system), see fig. 4.22.

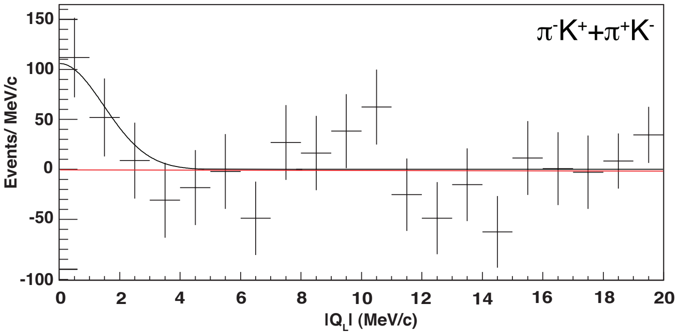

Figure 4.22: *Residuals between data and the fitted background for π^-K^+ and π^+K^-. A Gaussian fit has been applied (solid line) to illustrate the distribution of atomic-pairs.*

The statistical significance was only 3.2σ. However, the evidence was strengthened by the simultaneous observation of interacting unbound Coulomb-pairs from which the fraction of expected bound pairs could be calculated. The latter is in excellent agreement with the number of observed atoms. This result led to a lower limit for the mean life of πK-atoms of 0.8 fs in the 1s-state (confidence level of 90%), which could be translated into an upper limit of $|a_{1/2} - a_{3/2}| <$ 0.58 m_π^{-1} [6, 7].

More data was collected in 2008 – 2011 which is being analyzed. The total number of πK atoms will be around 600 in the final analysis and the significance about 5.3σ. This will lead to an uncertainty of about 25% on $|a_{1/2} - a_{3/2}|$.

In 2012 DIRAC also took data on the energy difference ΔE between the pionium $2p$- and $2s$-states according to the following method: The pionium atoms produced in the target interact with an applied electric field and some of them leave the target in the $2p$-state. The decay into $\pi^0\pi^0$ is forbidden from p-states and hence the main decay process is $2p - 1s$ radiative transition (with subsequent annihilation from $1s$ into $\pi^0\pi^0$). Thus the mean life of the atom in the $2p$-state is determined by radiative transition, $\tau(2p) \simeq$ 12 ps, which is much slower than annihilation from the $1s$-states. We refer to these $2p$-states as "long-lived" 2π atoms. One then measures the energy difference ΔE by observing the field dependence of the number of long-lived 2π atoms breaking up into $\pi^+\pi^-$ pairs in a second foil located downstream of the production target. This is a measurement of the combination $2a_0 + a_2$. Together with the measurements from the $1s$-state DIRAC should then be able to derive the $\pi\pi$ scattering lengths a_0 and a_2 separately.

Data taking for the DIRAC experiment was completed at the end of 2012 and the apparatus was subsequently dismantled.

References

[1] B. Adeva *et al.* (DIRAC Collaboration), Phys. Lett. **B 704** (2011) 24
[2] A. Benelli, EPJ Web of Conferences **37** (2012) 01011, doi: 10.1051/epjconf/20123701011
[3] B. Adeva *et al.* (DIRAC Collaboration), Nucl. Instrum. Methods in Phys. Res. **A 515** (2003) 467
[4] Y. Allkofer *et al.*, Nucl. Instr. Meth. in Phys. Res. **A 582** (2007) 497;
Y. Allkofer *et al.*, Nucl. Instr. Meth. in Phys. Res. **A 595** (2008) 84;
C. Amsler, Proc. of Science PoS EPS-HEP (2009) 078
[5] S. Horikawa *et al.*, Nucl. Instr. Meth. in Phys. Res. **A 595** (2008) 212
[6] B. Adeva *et al.* (DIRAC Collaboration), Phys. Lett. **B 674** (2009) 11
[7] Y. Allkofer, PhD Thesis, University of Zurich (2008)

5 Publications

Articles

1. The AEGIS experiment at CERN: Measuring the free fall of antihydrogen
   AEgIS Collaboration
   Hyperfine Interactions **209** (2012) 43
   doi: 10.1007/s10751-012-0583-x

2. Towards the production of an ultra cold antihydrogen beam with the AEGIS apparatus
   James William Storey
   Hyperfine Interactions **212** (2012) 109
   doi: 10.1007/s10751-011-0401-x

3. Study of nuclear recoils in liquid argon with monoenergetic neutrons
   C. Regenfus, Y. Allkofer, C. Amsler, W. Creus, A. Ferella, J. Rochet, M. Walter
   Journal of Physics: Conference Series **375** (2012) 012019
   doi:10.1088/1742-6596/375/1/012019

4. A new application of emulsions to measure the gravitational force on antihydrogen
   C. Amsler et al.
   J. of Instrumentation **8** (2013) P02015

5. Exploring the WEP with a pulsed cold beam of antihydrogen
   M. Doser, C. Amsler, et al. (AEgIS Collaboration)
   Classical Quantum Gravity **29** (2012) 184009
   doi: 10.1088/0264-9381/29/18/184009

6. The DIRAC experiment at CERN
   Angela Benelli (DIRAC Collaboration)
   EPJ Web of Conferences **37** (2012) 01011
   doi: 10.1051/epjconf/20123701011

7. Further Evidence for Low Energy Protonium Production in Vacuum
   E. Lodi Rizzini et al. (ATHENA Collaboration)
   Eur. Phys. J. **Plus** (2012) 127
   doi: 10.1140/epjp/i2012-12124-9

8. The Review of Particle Physics
   J. Beringer et al. (Particle Data Group)
   Phys. Rev. **D86** (2012) 010001

9. Note on scalar mesons below 2 GeV
   C. Amsler, S. Eidelman, T. Gutsche, C. Hanhart, S. Spanier and N. A. Törnqvist
   Phys. Rev. **D86** (2012) 706

10. The $\eta(1405)$, $\eta(1475)$, $f_1(1420)$, and $f_1(1510)$
    C. Amsler and A. Masoni
    Phys. Rev. **D86** (2012) 759

11. Quark Model
    C. Amsler, T. DeGrand and B. Krusche
    Phys. Rev. **D86** (2012) 199

12. Recent studies of top quark properties and decays at hadron colliders
    V. Chiochia
    Mod. Phys. Lett. **A 27** (2012) 1230036

Articles (CMS Collaboration)[1]

1. Observation of a New Ξ_b Baryon
   CMS Collaboration
   Phys. Rev. Lett. **108** (2012) 252002
2. Measurement of the $\Upsilon(1S)$, $\Upsilon(2S)$ and $\Upsilon(3S)$ polarizations in pp collisions at $\sqrt{s} = 7$ TeV
   CMS Collaboration
   Phys. Rev. Lett. **110** (2013) 081802
3. On the mass and spin-parity of the Higgs boson candidate via its decays to Z boson pairs
   CMS Collaboration
   Phys. Rev. Lett. **110** (2013) 081803
4. Search for the standard model Higgs boson decaying to bottom quarks in pp collisions at $\sqrt{s} =$ 7 TeV
   CMS Collaboration
   Phys. Lett. **B 710** (2012) 284
5. Search for the standard model Higgs boson decaying to bottom quarks in pp collisions $\sqrt{s} =$ 7 TeV
   CMS Collaboration
   Phys. Lett. **B 710** (2012) 284
6. Search for neutral Higgs bosons decaying to τ pairs in pp collisions $\sqrt{s} = 7$ TeV
   CMS Collaboration
   Phys. Lett. **B 713** (2012) 68
7. Measurement of the Λ_b cross section and the $\overline{\Lambda}_b$ to Λ_b ratio with $J/\psi\Lambda$ decays in pp collisions $\sqrt{s}$ = 7 TeV
   CMS Collaboration
   Phys. Lett. **B 714** (2012) 136
8. Observation of a new boson at a mass of 125 GeV with the CMS experiment at the LHC
   CMS Collaboration
   Phys. Lett. **B 716** (2012) 30
9. J/ψ and $\psi(2S)$ production in pp collisions at $\sqrt{s}$ = 7 TeV
   CMS Collaboration
   J. High Energy Phys. **02** (2012) 011
10. Search for $B^0_s \to \mu^+\mu^-$ and $B^0 \to \mu^+\mu^-$ decays
    CMS Collaboration
    J. High Energy Phys. **04** (2012) 033

---

[1] For CMS publications we list a selection of papers related to activities of our group. For a full CMS bibliography see http://cdsweb.cern.ch/collection/CMS

11. Inclusive b-jet production in pp collisions at $\sqrt{s}$ = 7 TeV
    CMS Collaboration
    J. High Energy Phys. **04** (2012) 084

12. Search for the standard model Higgs boson produced in association with W and Z bosons in pp collisions $\sqrt{s} = 7$ TeV
    CMS Collaboration
    J. High Energy Phys. **11** (2012) 088

13. Measurement of the cross section for production of $b\bar{b}X$, decaying to muons in pp collisions at $\sqrt{s}$ = 7 TeV
    CMS Collaboration
    J. High Energy Phys. **06** (2012) 110

14. Measurement of the relative prompt production rate of χ_{c2} and χ_{c1} in pp collisions at $\sqrt{s} =$ 7 TeV
    CMS Collaboration
    Eur. Phys. J. **C 72** (2012) 2251

15. A New Boson with a Mass of 125 GeV observed with the CMS Experiment at the Large Hadron Collider
    CMS Collaboration
    Science **338** (2012) 1569

Articles in press

1. Particle tracking at 4K: The Fast Annihilation Cryogenic Tracking (FACT) detector for the AEgIS antimatter gravity experiment
   J. Storey et al. (AEgIS Collaboration)
   Submitted to Nucl. Instr. and Meth.

2. Development of nuclear emulsions with 1 μm spatial resolution for the AEgIS experiment
   M. Kimura et al. (AEgIS Collaboration)
   Submitted to Nucl. Instr. and Meth.

3. Studies of rare B hadron decays to leptons at hadron colliders
   V. Chiochia
   arXiv:1302.2205

4. Search for a standard-model-like Higgs boson with a mass of up to 1 TeV at the LHC
   CMS Collaboration
   arXiv:1304.0213

5. Measurement of the $X(3872)$ production cross section via decays to $J/\psi\pi^+\pi^-$ in pp collisions at $\sqrt{s} = 7$ TeV
   CMS Collaboration
   arXiv:1302.3968

6. Measurement of the $\Upsilon(1S)$, $\Upsilon(2S)$ and $\Upsilon(3S)$ cross sections in pp collisions at $\sqrt{s} = 7$ TeV
   CMS Collaboration
   arXiv:1303.5900

7. Observation of a new boson with mass near 125 GeV in pp collisions at $\sqrt{s} = 7$ TeV
   CMS Collaboration
   arXiv:1303.4571

8. Search for a Higgs boson decaying into a b-quark pair and produced in association with b-quarks in proton-proton collisions at 7 TeV
   CMS Collaboration
   arXiv:1302.2892

9. Identification of b-quark jets with the CMS experiment
   CMS Collaboration
   arXiv:1211.4462

Lectures

1. Particle tracking at 4K: The Fast Annihilation Cryogenic Tracking (FACT) detector for the AEgIS antimatter gravity experiment
   Carlo Canali
   13th Vienna Conference on Instrumentation, Vienna, Austria, 11 February 2013

2. The DIRAC experiment at CERN
   Angela Benelli
   Meson 2012 Conference, Krakow, Poland, 1 June 2012

3. Measurements of top quark properties and decays at the Tevatron and LHC
   Vincenzo Chiochia
   Flavor Physics and CP violation conference, Hefei, China, 21 May 2012

4. Observation of a new Ξ_b baryon with the CMS experiment
   V. Chiochia
   Colloquium on Particle Physics, PSI, Villigen, Switzerland, 18 October 2012

5. Rare B decays at LHC and Tevatron
   V. Chiochia
   Hadron Collider Physics Symposium, Kyoto, Japan, 12 November 2012

6. Heavy flavor physics with the CMS experiment
   Vincenzo Chiochia
   Saha Institute for Nuclear Physics (Kolkata)
   Indian Institute of Technology and Tata Institute of Fundamental Research (Mumbai)
   5 – 8 March 2013

7. Heavy flavor production in association with vector bosons at CMS
   Simon de Visscher
   Workshop of the LHC Electroweak working group, CERN, 2 April 2012

8. Heavy flavor production in association with vector bosons in CMS
   Simon de Visscher
   36th International Conference on High Energy Physics, Melbourne, Australia, 4 July 2012

9. Angular correlation between B-hadrons produced in association with a Z boson at the CMS experiment

Carlotta Favaro
Swiss Physical Society, ETH-Zurich, 22 June 2012

10. Heavy flavor and vector bosons associated production at CMS
Carlotta Favaro
16th International Conference in Quantum Chromodynamics, Montpellier, France, 2 July 2012

11. Vector boson and heavy flavor associated production at CMS
C. Favaro
Lake Louise Winter Institute, Lake Louise, Canada, 17 February 2013

12. b-baryon studies at the CMS Experiment
Mirena Ivova Rikova
Swiss Physical Society, ETH-Zurich, 22 June 2012

13. Measurement of lifetime difference $\Delta\Gamma_s$ in the decay $B_s \to J/\psi\phi \to \mu^+\mu^-K^+K^-$
Barbara Millán Mejías
Swiss Physical Society, ETH-Zurich, 22 June 2012

14. Production of b hadrons and b-jet cross sections at CMS
H. Snoek
Heavy Flavor Production Workshop, Berkeley, USA, 14 January 2013

15. Search for 2HDM Higgs boson decaying into τ pairs at CMS
Mauro Verzetti
Swiss Physical Society, ETH-Zurich, 22 June 2012

AEgIS Collaboration (2013):
Bergen University, Bern University, CERN, Claude Bernard University (Lyon), Czech Technical University, ETH-Zürich, INFN: Brescia - Firenze - Genova - Milano - Padova - Pavia - Trento; INR (Moscow), ITEP (Moscow), Kirchhoff Institute of Physics (Heidelberg), Laboratoire Aimé Cotton (Orsay), MPI-K (Heidelberg), Oslo University, Politecnico Milano, Stefan Meyer Institut (Vienna), University College (London).

CMS Collaboration (2013):
see http://greybook.cern.ch/programmes/experiments/CMS.html

DARWIN Collaboration (2013):
Subatech, University of Münster, MPIK-Heidelberg, University of Karlsruhe, University of Mainz, TU-Dresden, Imperial College London, INFN (Italy): LNGS-Napoli-Padova-Pavia-Perugia-Milano-Bologna; Weizmann Institute of Science, Nikhef (Amsterdam), University of Zürich, University of Bern, ETH-Zürich, Columbia University, Princeton University, UCLA, Arizona State University, Purdue University.

DIRAC Collaboration (2013):
Bern University, Bucharest, CERN, Czech Technical University, FZU-IP ASCR (Prague), INFN: Frascati-Messina-Trieste; IHEP-Protvino, JINR (Dubna), KEK, Kyoto Sangyo University, SINP (Moscow), Tokyo Metropolitan University, Zürich University.

PARTICLE DATA Group (2013):
see http://pdg.lbl.gov/2012/html/authors_2012.html